

How cells regulate the type and size of actin structures

Ondrej Maxian

October 5, 2023

The goal of this write-up is to explore how modeling can help us understand *in vivo* regulation of actin structure and size. We focus on the two predominant types of actin networks: branched structures (which tend to condense into endocytic patches sometimes referred to as “mini-comets”), and linear structures (which form filopodia and the contractile ring). The branched structures are mediated by the arp 2/3 complex, which binds to existing mother filaments to form branches [12], while the latter are mediated by formins, which makes screw-like rotations to allow monomers to enter [16, 7]. Our research question is as follows: how does the cell regulate the type and size of branched vs. linear actin structures, while at the same time preserving the total amount of actin in the cell?

1 Introduction

To assemble filaments, actin monomers associate with diffusion-limited rate constant [12]. The barbed end elongation rate has been measured as $= k_{\text{on}}G$, where G is concentration of G actin and $k_{\text{on}} = 11.6 \mu\text{M}^{-1} \text{ s}^{-1}$ [17]. As the dissociation rate is not a function of bulk concentration, an equilibrium exists around bulk concentration of $0.1 \mu\text{M}$ where a fixed percentage of actin is in monomeric form, with the rest in polymerized form. While the total amount of incorporated actin is therefore fixed, the kinetics leave undetermined how much is in branched vs. filamentous form. To control this, the conventional viewpoint is that external or internal signals activate signaling cascades which eventually cause the cell to produce more or less of a particular type of network [9, 12, 17]. However, recent experimental evidence has shown that a limiting actin pool must also control the types of structures being produced.

Experiments show that depleting the arp 2/3 complex leads to more filamentous actin networks [15]. Specifically, in fission yeast, inhibition of arp 2/3 by the drug CK-666 leads to new assembly of F-actin, as long as there is sufficient formin present. Subsequent washing out of CK-666 gives

disassembly of the “ectopic” F-actin and reassembly of dense actin patches [1], indicating that the release of F-actin via disassembly is important for the assembly of new structures [17]. On the opposite end, formin depletion also enhances arp 2/3-mediated assembly. In single mutant formin cells, the density of endocytic actin patches is roughly doubles, but the size and lifetime of the patches remains the same [1]. This suggests that the mechanism of size control is independent from the mechanism of choosing filamentous vs. branched structures.

The most curious experimental observations have to do with changes in structure when the actin pool changes. If the structures are a function only of the arp 2/3 and formin concentrations, then we would expect changes in actin concentration to decrease each kind of structure in the same proportion. However, experiments in fission yeast show that underexpression of actin favors formin-mediated contractile rings, while overexpression favors arp 2/3 complex mediated actin patches [1]. These observations imply that the cell assembles formin-mediated structures “first” in some sense, and then assembles arp 2/3 structures with the excess actin. But it isn’t clear what is meant by “first” here.

There are additional confounding agents that could tip the scales in one direction or the other. We focus on two: profilin and capping protein. In general, the presence of profilin correlates with more filamentous actin structures [17], as actin binding to profilin prevents filament nucleation but allows for barbed end growth [12]. Depletion of capping protein increases arp 2/3-mediated patches by at least 35% [17]. This is confusing because capping protein competes with formin for barbed ends [6], and so we would expect depleting capping protein to increase formin levels and lead to more filamentous actin.

The modeling that has been done on this problem has so far been limited to the size control of a generic filamentous actin structure, and has been carried out extensively by Kondev and collaborators. Their results can be summarized as follows: when there is competition for a finite pool of subunits, only one quantity is well-defined, the *total* amount of monomer that is found in filamentous form. This means that the length distribution of individual filaments (or structures) is not well defined [11, 5]. In addition, the limiting pool hypothesis by itself predicts that structures with slightly higher on rates will capture all of the monomers at equilibrium. Applying to our problem, their limiting pool model predicts either stochastic swings between branched and filamentous actin (if the on rates are the same), or all of the actin in the structure with faster on rate. Neither of these is what we see *in vivo*, where the balance between branched and filamentous actin is maintained at a relative steady state in time.

Because these models are steady state models, it is certainly possible that the intermediate filament lengths are quasi-stable, and that the drift to steady state occurs on very long timescales [18]. Alternative ideas are covered in recent extensions of Kondev’s models [10], which have shown that the correct length distribution of yeast actin cables can be predicted by consider length-dependent attachment rates, as well as sensing of the cell boundaries. Additional work [13] has shown that considering filaments as part of bundles, whose longest fiber sets the length of the bundle, is able to explain the variance of fiber length in actin bundles.

1.1 The key questions

It’s clear from these observations that the partitioning between branched and filamentous actin structures is a function of three variables: (1) the bulk actin concentration, (2) the arp 2/3 concentration, and (3) the formin concentration. What we want to use modeling to understand is *how* these three agents combine to generate steady state structures, and in particular explain the following experimental observations

1. Less arp 2/3 gives more filamentous actin structures.
2. Less formins give more branched structures.
3. Underexpression of actin gives more filamentous structures.
4. Overexpression of actin gives more branched structures.

1.2 A modeling plan

An ideal modeling study would consist of the following procedure:

1. Begin with a small system of *discrete* formin, arp 2/3, and actin molecules, which diffuse around randomly.
2. Formulate a set of interaction rules by which reactions occur between these.
3. See if those rules generate the correct steady states qualitatively.
4. Formulate a set of ODEs from the microscopic simulations that describes the interactions.

There is a separate issue of the size control of the individual structures. Because manipulating actin, arp 2/3, and formin concentration keeps the size of the structures the same, this likely occurs by different mechanisms, and is something we can look at later.

2 Diffusion

The first thing we do in building up our model is to consider the diffusion of an actin structure with arbitrary configuration. We will assume that the actin structures are

1. Made of N spheres of radius a
2. Moving as rigid bodies

2.1 Kinematics and mobility

Let us denote the structure by the array \mathbf{X} . When moving as a rigid body, the structure has velocity

$$\mathbf{U} = \mathbf{U}_{\text{COM}} + \boldsymbol{\Omega} \times (\mathbf{X} - \mathbf{X}_{\text{COM}}) := \mathbf{K}[\mathbf{X}]\boldsymbol{\alpha} \quad (1)$$

where $\mathbf{X}_{\text{COM}} = N^{-1} \sum \mathbf{X}_p$ denotes the center of mass and \mathbf{U}_{COM} denotes the velocity of the center of mass. Following the formulation in [2], the mobility matrix which relates the total force and torque on the body to its translational and angular velocity is given by

$$\mathbf{N} = (\mathbf{K}^T \mathbf{M}^{-1} \mathbf{K})^\dagger, \quad (2)$$

where \dagger denotes the pseudo-inverse and $\mathbf{M} = \mathbf{I}/(6\pi\mu a)$ is the mobility of the particles absent the constraint (\mathbf{M}^{-1} is the drag coefficient). Here we are not incorporating any hydrodynamics, so the mobility is simply

$$\mathbf{N} = \frac{1}{6\pi\mu a} (\mathbf{K}^T \mathbf{K})^\dagger = \begin{pmatrix} \mathbf{N}_{\text{tt}} & \mathbf{0} \\ \mathbf{0} & \mathbf{N}_{\text{rr}} \end{pmatrix}. \quad (3)$$

Here there is no coupling between rotation and translation when we measure the mobility about the center of mass. This is a consequence of using the simple hydrodynamic mobility; see [2, Sec. IV(A)] for more discussion.

2.2 Langevin equation

The Ito Langevin equation describing diffusion of the body is given by [8]

$$d \begin{pmatrix} \mathbf{X}_{\text{COM}} \\ \boldsymbol{\tau} \end{pmatrix} = \sqrt{2k_B T} \mathbf{N}^{1/2} d\mathbf{W}, \quad (4)$$

where $d\mathbf{W}$ is a 6-vector of Brownian motion increments with the property $\langle d\mathbf{W} d\mathbf{W}^T \rangle = \mathbf{N} \Delta t$, and $\boldsymbol{\tau}$ describes any material vector attached to the body. Note that there are no stochastic drift terms

because the mobility is measured about the center of mobility [8]. Still not quite written correctly.

A numerical method to solve this equation is to [2]

1. Compute $\mathbf{N}[\mathbf{X}]$

2. Set

$$\begin{pmatrix} \mathbf{U}_{\text{COM}} \\ \mathbf{\Omega} \end{pmatrix} = \boldsymbol{\alpha} = \sqrt{\frac{2k_B T}{\Delta t}} \mathbf{N}^{1/2} \boldsymbol{\xi},$$

where $\boldsymbol{\xi}$ is a vector of six standard i.i.d. Gaussian random numbers.

3. Evolve the center of mass by $\mathbf{X}_{\text{COM}}^{(n+1)} = \mathbf{X}_{\text{COM}}^{(n)} + \Delta t \mathbf{U}_{\text{COM}}$ and rotate the tangent vectors of each fiber by $\mathbf{\Omega} \Delta t$.

In practice, because of (de)polymerization, it will be more practical to track the endpoint \mathbf{X}_0 . So, we update the center of mass and evolve the tangent vectors, then compute a new \mathbf{X}_0 via

$$\mathbf{X}_0^{(n+1)} = \mathbf{X}_{\text{COM}}^{(n+1)} + \text{rotate}(\mathbf{X}_0^{(n)} - \mathbf{X}_{\text{COM}}^{(n)}, \Delta t \mathbf{\Omega})$$

2.3 Theory

We now examine the translational and rotational diffusion of particles in free space, for which we have theoretical results [8]. Let $\Delta \mathbf{X}_c(t) = \mathbf{X}_{\text{COM}}(t) - \mathbf{X}_{\text{COM}}(0)$, then

$$\langle \Delta \mathbf{X}_c(t) \cdot \Delta \mathbf{X}_c(t) \rangle = 2k_B T \text{trace}(\mathbf{N}_{\text{tt}}) t. \quad (5)$$

Likewise, let \mathbf{u}_1 be the eigenvector of \mathbf{N}_{rr} with maximum eigenvalue, and suppose that we express \mathbf{u}_1 in terms of the material frame at $t = 0$. Then

$$\langle \mathbf{u}_1(t) \cdot \mathbf{u}_1(0) \rangle = e^{-\alpha t} \quad \alpha = k_B T (\lambda_2 + \lambda_3), \quad (6)$$

where λ_2 and λ_3 are the two smallest eigenvalues of \mathbf{N}_{rr} .

In all simulations in this section, we set $k_B T = 4.1 \times 10^{-3}$ pN $\cdot\mu\text{m}$, $a = 0.004$ μm and $\mu = 1$ Pa $\cdot\text{s}$.

2.4 Monomers

In the case of monomers, there is no rotational diffusion, $\mathbf{N}_{\text{tt}} = 1/(6\pi\mu a)$ and (5) simplifies to

$$\langle \Delta \mathbf{X}_c(t) \cdot \Delta \mathbf{X}_c(t) \rangle = \frac{k_B T}{\pi\mu a} t \quad (7)$$

In Fig. 1, we perform simulations with 1000 monomers, repeated 10 times to generate error bars. We observe perfect agreement between our simulation and theory.

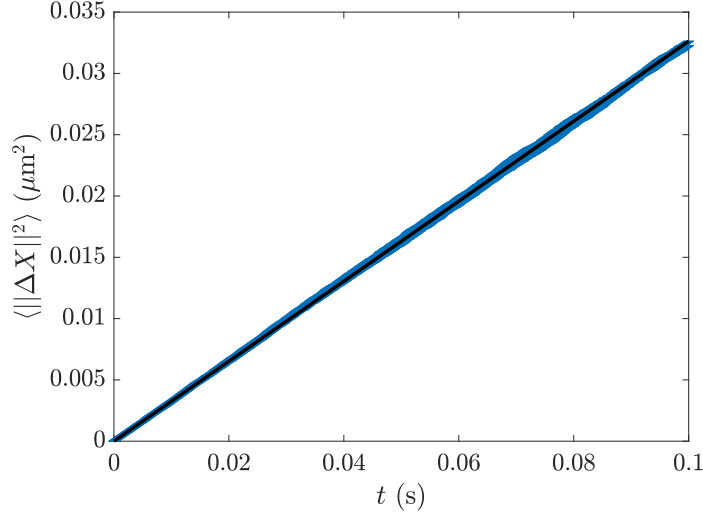


Figure 1: Diffusion of monomers. The blue line shows the MSD as a function of time, and the black line shows the theory (7).

2.5 Fibers

Continuing on to linear fibers, we perform simulations with 10 fibers, repeated 10 times to generate error bars. Each fiber contains 10 monomers. The results in Fig. 2 show agreement between simulations and theory.

2.6 Branched fibers

We have a lot of freedom for branched fibers. We fix the geometry as shown in Fig. 3. There are 18 monomers here, 10 on the longest fiber, then 5 on the one attached, and then 3 on the small output. As before, we simulate this fiber 10 times to generate a mean, then repeat this 10 times to generate error bars. Results in Fig. 4 show agreement between experiments and theory.

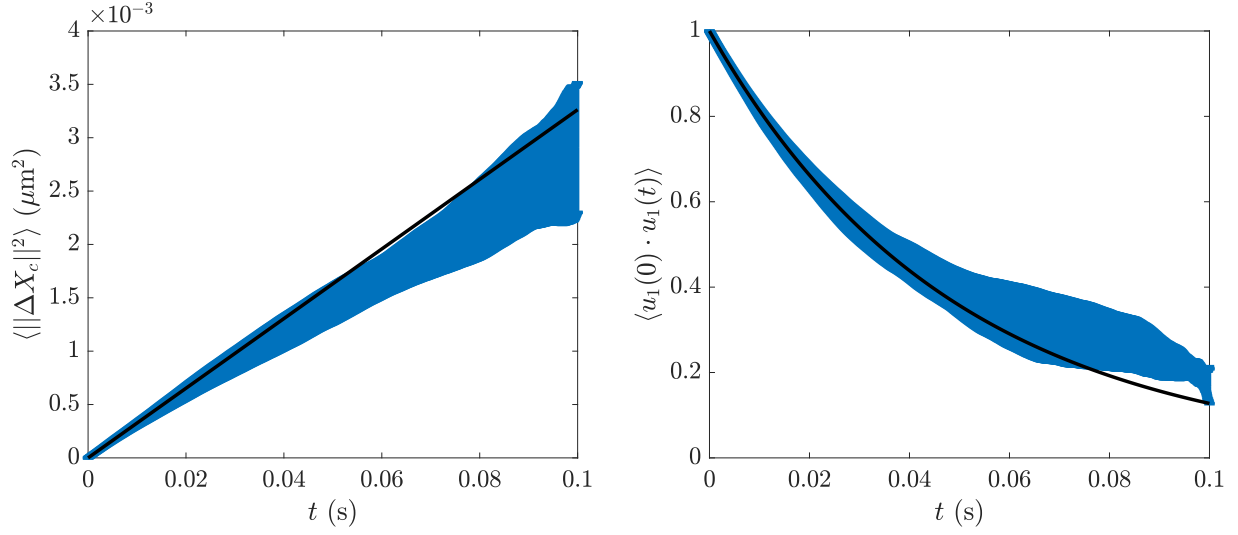


Figure 2: Diffusion of linear fibers. The left plot shows translational diffusion, for which we compare the data in blue to the theory (5) in black, while the right plot shows rotational diffusion, for which we compare the data in blue to the theory (6) in black.

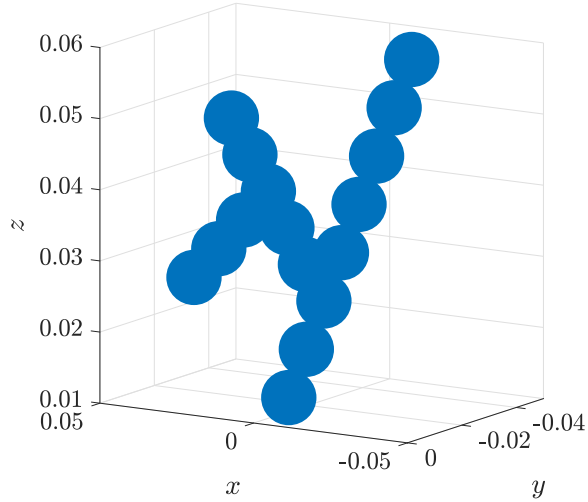


Figure 3: The branched fiber we use for our diffusion test. Axis is in μm .

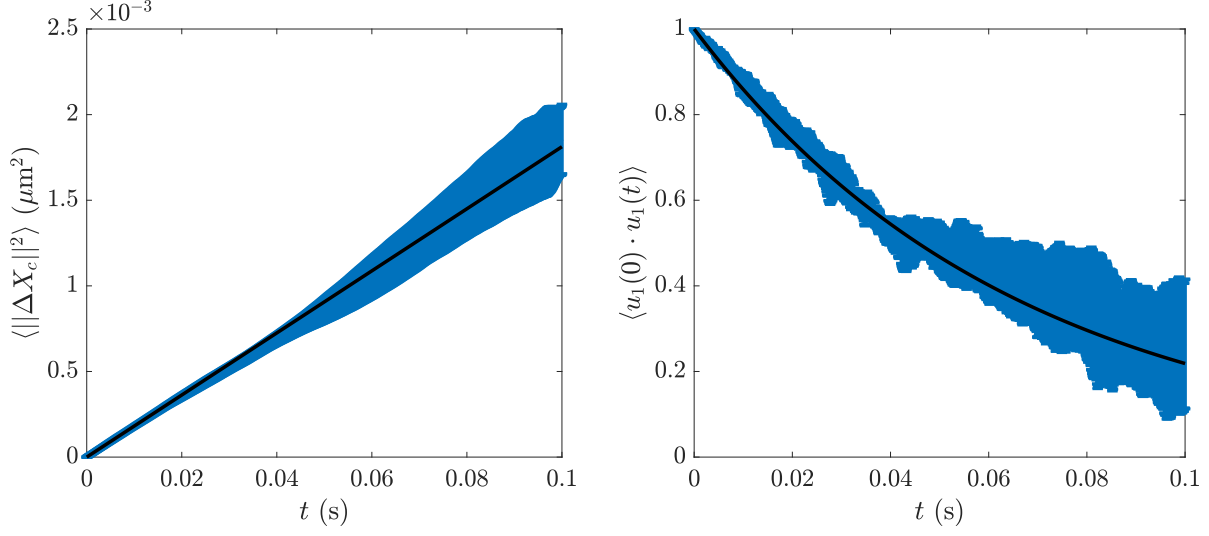


Figure 4: Diffusion of branched fibers. The left plot shows translational diffusion, for which we compare the data in blue to the theory (5) in black, while the right plot shows rotational diffusion, for which we compare the data in blue to the theory (6) in black.

3 Linear fiber reactions

To begin, we will restrict our reaction kinetics to a system of monomers and *linear* fibers. The formation of a “fiber” will occur with two monomers, after which we add monomers to the pointed and barbed ends. There are therefore six reactions in our system:

1. Two monomers becoming a fiber of length two: $A + A \xrightarrow{\lambda_m} A_2$. This reaction occurs (with rate λ_m (units 1/time)) if two monomers are within a distance R_{rxn} of each other. In this case, we choose one of the two monomers at random as the fiber “starting point,” then choose a random tangent vector τ on the unit sphere. The second monomer is inserted a fixed spacing $\Delta s = 2a$ apart in this direction τ .
2. A two-monomer fiber becoming two individual monomers: $A_2 \xrightarrow{\nu_m} A + A$. This reaction occurs with rate $\nu_m = \nu_b + \nu_p$ (units 1/time; see reaction 4 for definition of ν_b and ν_p), and is the reverse of the binding reaction. We choose one monomer at random to keep in place, then set the location of the other one in a random location inside of the reactive sphere of radius R_{rxn} centered around the first (fixed) particle.
3. A fiber adding to its barbed/pointed end: $A + A_n \xrightarrow{\lambda_{b/p}} A_{n+1}$. This reaction occurs with the corresponding rate at each end if the monomer A is within the reactive sphere of radius R_{rxn} .

4. A fiber depolymerizing from its barbed/pointed end: $A_n \xrightarrow{\nu_{b/p}} A_{n-1} + A$. If this reaction occurs, we place the new monomer A randomly in the reactive sphere of radius R_{rxn} centered around the barbed/pointed end of the fiber.

To process these reactions efficiently, at the beginning of each time step we construct a list of all actin monomers that are within R_{rxn} of each other (this list includes monomers that are bound to fibers). Then, we process all possible *binding* reactions. By “process,” we simply loop through the list of pairs of monomers. A reaction can occur between two monomers if they are either (a) both monomers or (b) one is a monomer and one is at the pointed/barbed end. If the reaction has rate λ , it occurs if $r < \lambda\Delta t$, where r is a random number from the uniform distribution $U[0, 1]$ and Δt is the time step over which we evolve the reaction network. After processing the binding reactions, we then repeat for the unbinding reactions. We note that this first order way of treating the reactions avoids the complication of having to update neighbor lists when particles bind and unbind from fibers (see [3] for such a treatment).

3.1 Free monomers and two-monomer “fibers”

As a first step toward validating the code and an exercise in computing macroscopic reaction rates from microscopic ones, we consider a simplified network where $\lambda_{b/p} = 0$; i.e., where two-monomer fibers cannot add to their barbed/pointed ends. The monomers therefore cycle between dimers and free monomers, which can be described by the *macroscopic* equilibrium

$$k^- c_{A_2} = k^+ c_A^2 \tag{8a}$$

$$2c_{A_2} + c_A = c_0, \tag{8b}$$

where c_0 represents the total actin concentration. This is a system of two equations for the unknowns c_A and c_{A_2} and ultimately results in solving the quadratic equation

$$k^+ c_A^2 + \frac{k^-}{2} c_A - \frac{k^- c_0}{2} = 0 \tag{9}$$

for c_A . The steady state concentration of dimers is then given by $c_{A_2} = (c_0 - c_A)/2$. Our goal is to verify that this is what our code outputs.

3.1.1 Macroscopic rate constants from microscopic ones

Prior to doing this, we need to determine how to extract the constants k^- (units 1/time) and k^+ (units volume/time) from the microscopic parameters. The first of these is simple; since the

macroscopic depolymerization and microscopic depolymerization are the same process, we have $k^- = \nu_m$. The same is not true of polymerization, since k^- describes the speed at which monomers diffuse to find other monomers *and* react to generate a dimer.

In the case of low densities, the macroscopic reaction rate is related to the microscopic rate via [4]

$$k^+ := k_0^+ = 2\pi D R_{\text{rxn}} \left(1 - \sqrt{\frac{D}{\lambda_m R_{\text{rxn}}^2}} \tanh \left(\sqrt{\frac{\lambda R_{\text{rxn}}^2}{D}} \right) \right). \quad (10)$$

As an approximation, we will set the diffusion coefficient $D = 2k_B T / (6\pi\mu a)$ to be equal to that of the *monomers*, although the dimers will diffuse slightly slower.

For finite packing densities, the nature of the process is fundamentally different depending on if it is reaction limited or diffusion limited, as discussed in [3]. The boundary between the two is defined by the dimensionless number

$$r = \frac{\lambda_m R_{\text{rxn}}^2}{D} = \lambda_m R_{\text{rxn}}^2 \frac{2k_B T}{6\pi\mu a}, \quad (11)$$

where $r \ll 1$ denotes a reaction-limited process and $r \gg 1$ is a diffusion-limited process. In the case when the process is reaction-limited, the system is mixed uniformly, and the rate of the forward reaction is simply the probability of finding a molecule in the reactive sphere of radius R_{rxn} (which equals $V_{\text{rxn}} c_A$), times the rate that the reaction occurs (equal to λ), times the number of A molecules in the system. This results in a forward rate constant [3, Eq. (2)]

$$k^+ = k_{\text{mix}} = \frac{1}{2} \frac{4\pi}{3} R_{\text{rxn}}^3 \lambda. \quad (12)$$

The case of diffusion-limited reactions at finite packing density is more complicated, and there are only empirical results for different algorithms in the literature. Our view is that if we verify our algorithm on reaction-limited processes, and confirm that it works for diffusion-limited processes at low densities, this is sufficient to declare it validated.

3.1.2 Simulation results in well-mixed systems

We set up a system of 1000 monomers inside of a $1 \mu\text{m}^3$ volume, which corresponds to a concentration of about $1.6 \mu\text{M}$ ($1 \mu\text{M} = 602$ molecules per μm^3), but a packing fraction of $\phi = 2.7 \times 10^{-4}$, so that the system is quite dilute and the formula (10) should still work well. For reaction rates, we fix $\lambda_m = 10$, $\nu_b = 5$, and $\nu_p = 7$ (so that $\nu_m = 12$) s^{-1} , and keep our typical units of $k_B T = 4.1 \times 10^{-3}$ $\text{pN} \cdot \mu\text{m}$, $a = 0.004 \mu\text{m}$, with $R_{\text{rxn}} = 10a$ (this reaction radius is artificially large to generate more

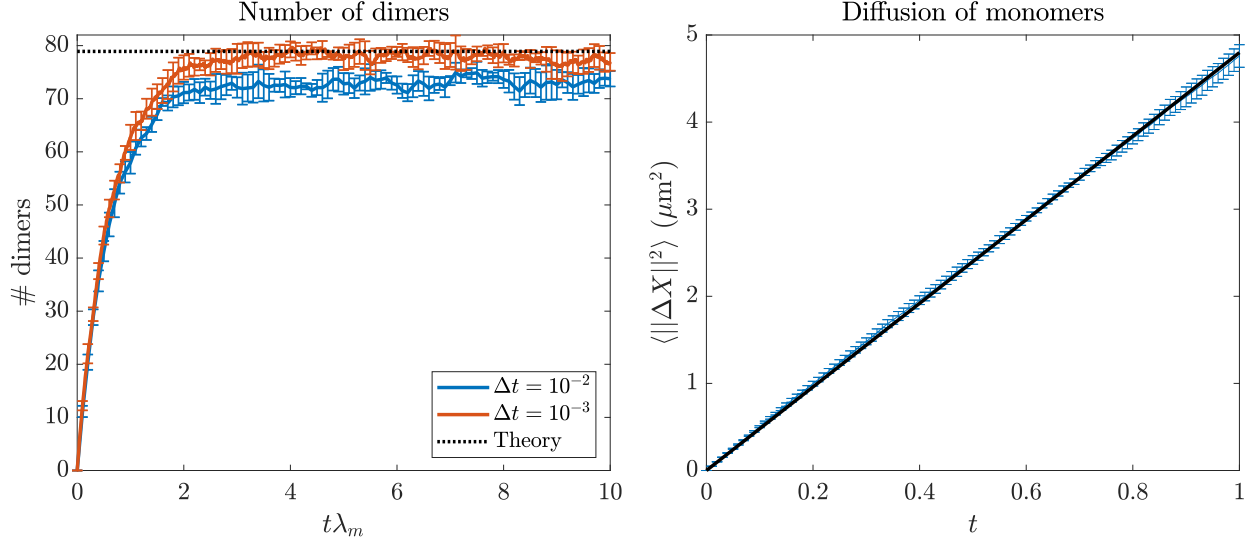


Figure 5: Verifying we obtain the correct mean number of dimers when the system is reaction limited. We consider only monomers and dimers with the parameters detailed at the start of Section 3.1.2, and set $\mu = 0.068$, so that $r = 0.01$ in (11). Left: the number of dimers over time in our algorithm with two different Δt values (the smaller $\Delta t = 10^{-3}$ has smaller errors). We compare to the theoretical value obtained by solving (9) in black. Right: diffusion of the monomers vs. the theory, confirming that, in this regime, reaction is *not* enhancing diffusion.

dimers). We then use the system viscosity as a control knob to tune the reaction-diffusion limited nature of the system.

We begin with the viscosity $\mu = 0.068$ Pa·s, so that $r = 0.01$ in (11). In this case the result of (10) for the forward rate k^+ is indistinguishable from the well-mixed case (12), and the solution of (9) is $c_{A_2} = 78.9$ in both cases. In Fig. 5, we verify that our algorithm gives this mean as the time step size shrinks to 0. To do this, we generate 10 trajectories to obtain a mean number of dimers, then repeat five times to generate error bars. A confidence interval is obtained by averaging over the last half of the trajectory (which from Fig. 5 is clearly in steady state), for which we obtain $c_{A_2} = 73.2 \pm 0.7$ for $\Delta t = 10^{-2}$ and $c_{A_2} = 77.8 \pm 0.7$ for $\Delta t = 10^{-3}$. This establishes that our algorithm gives the correct result in the reaction-limited case (at least within statistical errors).

3.1.3 When reaction enhances diffusion

Moving onto cases which are not diffusion limited, we increase the viscosity to $\mu = 0.68$, so that $r = 0.1$ in (11). We repeat the same test as in Fig. 5 and show the results in Fig. 6. This time, we see a deviation from expectations, as we obtain the confidence intervals $c_{A_2} = 71.9 \pm 0.3$ for

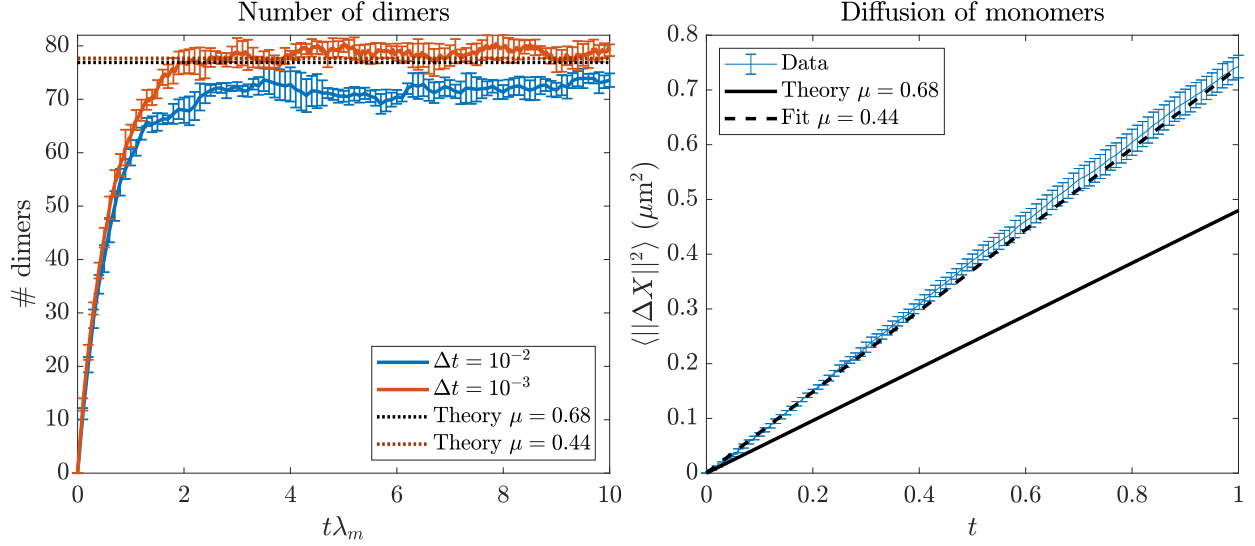


Figure 6: Increasing viscosity to $\mu = 0.68$ so that $r = 0.01$ in (11). We show the same quantities as in Fig. 5. Left: the number of dimers over time in our algorithm with two different Δt values (the smaller $\Delta t = 10^{-3}$ has smaller errors). We compare to the theoretical value obtained by solving (9) in black. Right: diffusion of the monomers vs. the theory. This time, we see enhanced diffusion by about a factor of 1.5; this has the effect of decreasing the viscosity by about 1.5.

$\Delta t = 10^{-2}$ and $c_{A_2} = 78.7 \pm 1.5$ for $\Delta t = 10^{-3}$, while the theoretical value is 76.9, which is slightly outside our confidence interval as $\Delta t \rightarrow 0$.

The errors we make can be understood in terms of the enhanced diffusion we obtain from reactions. In the right panel of Fig. 6, we plot the diffusion of the monomers over time, observing significantly larger displacement over the theoretical expectation when $\mu = 0.68$. In particular, the diffusion coefficient is enhanced by a factor of about 1.5 (in terms of absolute, the diffusion coefficient increases by $0.25 \mu\text{m}^2/\text{s}$). When we obtain a new viscosity from this, we get $\mu = 0.44$, which we see is a better fit (predicted $\#$ of dimers is 77.7) to our data, although we show in Fig. 7 that the diffusion we get from reaction alone is not of the form $\Delta X^2 \propto t$.

We note that there is a huge problem with this algorithm if we actually want to simulate the diffusion-limited regime. The enhancement of the diffusion coefficient scales like $R_{\text{rxn}}^2 \lambda_m$, but the ratio in (11) has precisely this in the numerator! So, the ratio r is bounded above by 1 using this numerical method, and we cannot simulate the diffusion-limited regime.

To understand if this is important, an actin monomer has diffusion coefficient $13.7 \mu\text{m}^2/\text{s}$, while the reaction radius is at most $0.01 \mu\text{m}^2$. Then the reaction rate would have to be 1370/s just to reach $r = 0.01$, which is unrealistically large. So it seems that the well-mixed assumption is a good

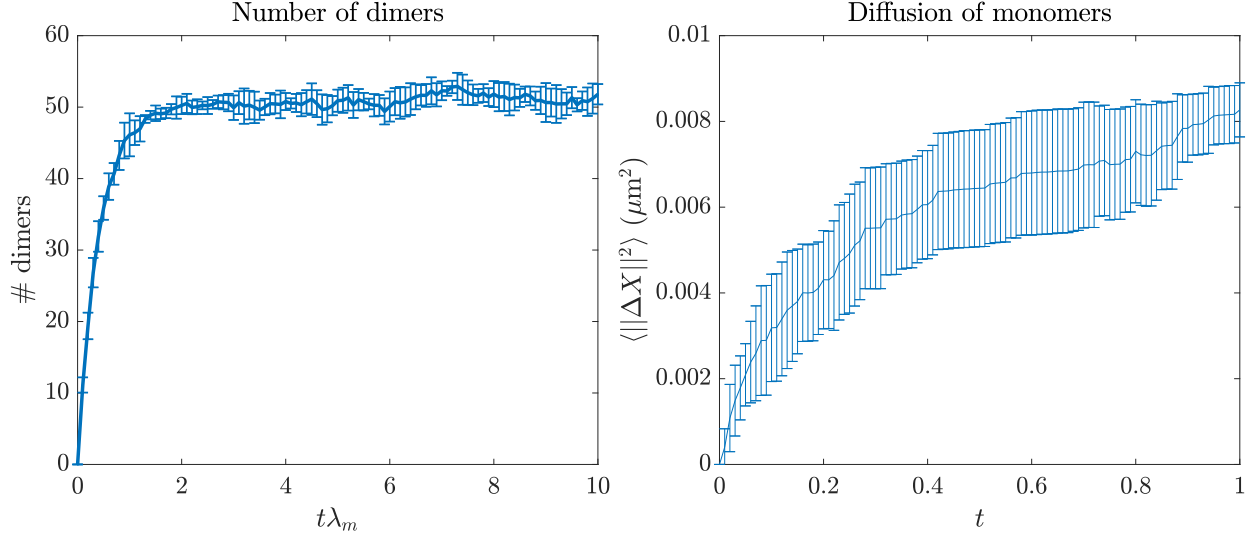


Figure 7: Same plot as Fig. 6, but without any diffusion. This illustrates the enhanced diffusion we obtain from reactions.

one for this system, and we can move on in the well-mixed regime.

3.2 Up to five monomers

Let us now suppose that we can have fibers with up to five monomers in them. Then the system of equations we need to solve is

$$k_f^- c_{A_5} = k_f^+ c_{A_4} c_A \quad (13a)$$

$$k_f^- c_{A_4} = k_f^+ c_{A_3} c_A \quad (13b)$$

$$k_f^- c_{A_3} = k_f^+ c_{A_2} c_A \quad (13c)$$

$$k_d^- c_{A_2} = k_d^+ c_A^2 \quad (13d)$$

$$5c_{A_5} + 4c_{A_4} + 3c_{A_3} + 2c_{A_2} + c_A = c_0. \quad (13e)$$

Here $k_f^- = k_p^- + k_b^-$ is the rate at which polymers lose a monomer from the pointed or barbed end, and $k_f^+ = k_p^+ + k_b^+$ is the rate at which monomers are added at the pointed/barbed end. In the well-mixed regime, the rate constants are given from the binding and unbinding rates as

$$k_d^+ = \frac{1}{2} \frac{4\pi}{3} R_{\text{rxn}}^3 \lambda_m \quad k_d^- = \nu_m \quad k_f^+ = \frac{4\pi}{3} R_{\text{rxn}}^3 (\lambda_b + \lambda_p) \quad k_f^- = \nu_b + \nu_p. \quad (14)$$

We again consider 1000 monomers with $a = 0.004$, $k_B T = 4.1 \times 10^{-3}$, and $\mu = 0.068$, and set the rates according to $\lambda_m = 12$, $\nu_m = 5$, $\lambda_b = 2$, $\lambda_p = 4$, $\nu_b = 1.5$, and $\nu_p = 2.5$. We again use

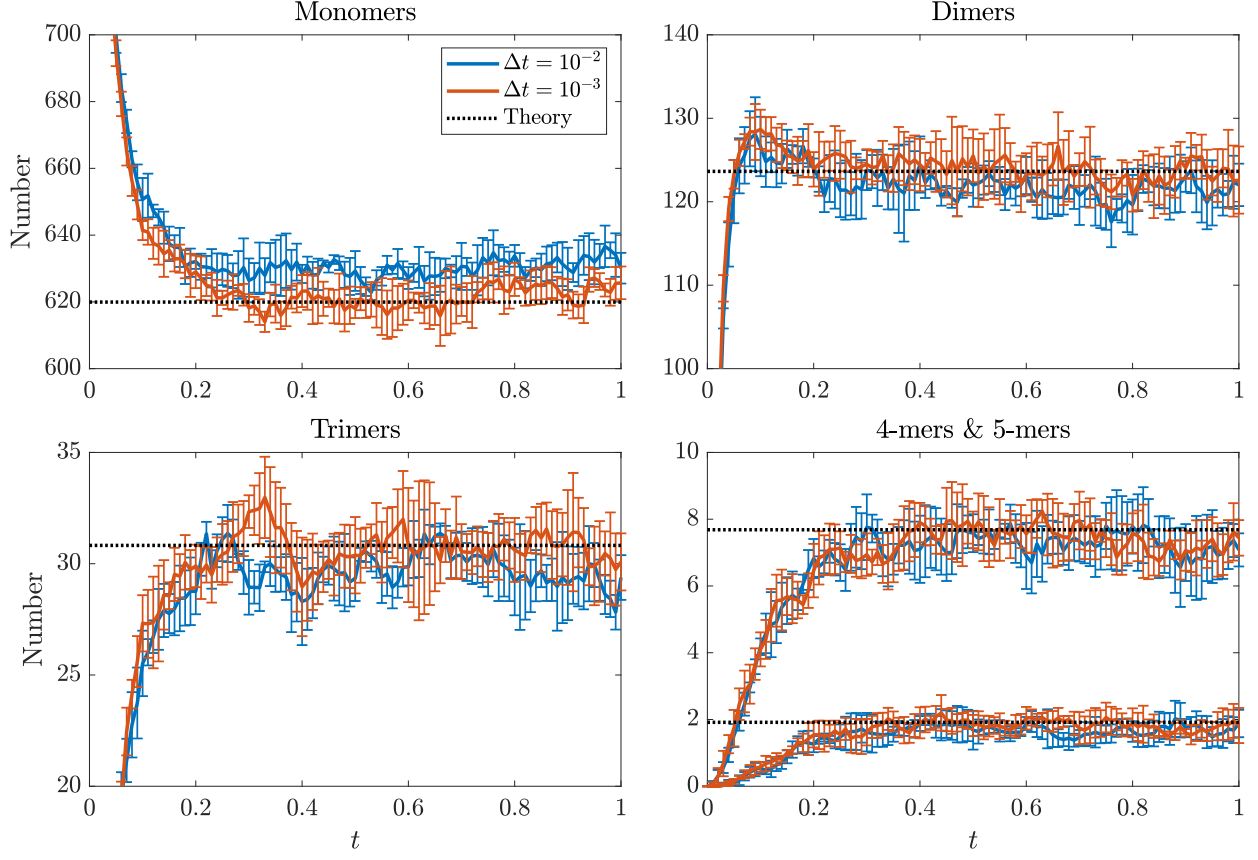


Figure 8: Steady state for fibers with up to five monomers. Theory is the solution of (13) with rate constants given by (14). The parameters we use are $\lambda_m = 12$, $\nu_m = 5$, $\lambda_b = 2$, $\lambda_p = 4$, $\nu_b = 1.5$, and $\nu_p = 2.5$.

the artificially large $R_{\text{rxn}} = 2.5a$. Figure 8 confirms that our numerical method gives the correct results in the well-mixed regime.

3.3 Using the real actin parameters

Let us now consider the same simulation, but with the parameters equal to those for actin, given in Table 1. This simulation is more demanding because there is a separation of timescales in the pointed and barbed end addition rates, compared to the reaction of two monomers. The only simplification we make in Table 1 is to consider a nucleate as comprising two monomers, as opposed to the three in [14]. This actually speeds up the rate of filament formation, since we skip the equally slow trimer formation step.

If we again allow a maximum of five monomers per fiber, and have 1000 total monomers, the steady state number of fibers (rounded to the nearest whole number) is (784, 0, 1, 5, 39). We now

Parameter	Description	Value	Units	Ref	Notes
a	Actin diameter	4	nm		One diameter $D = 2k_B T / (6\pi\mu a) \approx 11 \mu\text{m}^2/\text{s}$
R_{rxn}	Reaction radius	8	nm		
$k_B T$	Thermal energy	4.1×10^{-3}	pN $\cdot\mu\text{m}$		
μ	Fluid viscosity	0.01	Pa $\cdot\text{s}$		
k_d^+	Dimer formation rate	3.5×10^{-6}	$\mu\text{M}^{-1}\cdot\text{s}^{-1}$	[14]	$1 \mu\text{M}=602.2 \mu\text{m}^{-3}$
k_d^+	Dimer formation rate	5.8×10^{-9}	$\mu\text{m}^3\cdot\text{s}^{-1}$	[14]	
λ_m	Rate of 2 monomer reaction	5.4×10^{-3}	s^{-1}	(14)	
$k_d^- = \nu_m$	Dimer dissociation rate	0.041	s^{-1}	[14]	
k_b^+	Barbed end addition rate	11.6	$\mu\text{M}^{-1}\cdot\text{s}^{-1}$	[14]	$1 \mu\text{M}=602.2 \mu\text{m}^{-3}$
k_b^+	Barbed end addition rate	0.019	$\mu\text{m}^3\cdot\text{s}^{-1}$	[14]	
λ_b	Barbed end reaction rate	9.0×10^3	s^{-1}	(14)	
$k_b^- = \nu_b$	Barbed end dissociation rate	1.4	s^{-1}	[14]	
k_p^+	Pointed end addition rate	1.3	$\mu\text{M}^{-1}\cdot\text{s}^{-1}$	[14]	$1 \mu\text{M}=602.2 \mu\text{m}^{-3}$
k_p^+	Pointed end addition rate	2.2×10^{-3}	$\mu\text{m}^3\cdot\text{s}^{-1}$	[14]	
λ_p	Pointed end reaction rate	1.0×10^3	s^{-1}	(14)	
$k_p^- = \nu_p$	Pointed end dissociation rate	0.8	s^{-1}	[14]	

Table 1: Parameter values.

see what time step we need to take to reproduce this. To speed things up, we start the configuration in steady state.

References

- [1] Thomas A Burke, Jenna R Christensen, Elisabeth Barone, Cristian Suarez, Vladimir Sirotkin, and David R Kovar. Homeostatic actin cytoskeleton networks are regulated by assembly factor competition for monomers. *Current Biology*, 24(5):579–585, 2014.
- [2] Steven Delong, Florencio Balboa Usabiaga, and Aleksandar Donev. Brownian dynamics of confined rigid bodies. *The Journal of chemical physics*, 143(14), 2015.
- [3] Aleksandar Donev, Chiao-Yu Yang, and Changho Kim. Efficient reactive brownian dynamics. *The Journal of chemical physics*, 148(3), 2018.
- [4] Radek Erban and S Jonathan Chapman. Stochastic modelling of reaction–diffusion processes: algorithms for bimolecular reactions. *Physical biology*, 6(4):046001, 2009.
- [5] David Harbage and Jané Kondev. Exact length distribution of filamentous structures assembled from a finite pool of subunits. *The Journal of Physical Chemistry B*, 120(26):6225–6230, 2016.
- [6] David R Kovar, Jian-Qiu Wu, and Thomas D Pollard. Profilin-mediated competition between capping protein and formin cdc12p during cytokinesis in fission yeast. *Molecular biology of the cell*, 16(5):2313–2324, 2005.
- [7] Xi Li and Bin Chen. How torque on formins is relaxed strongly affects cellular swirling. *Biophysical Journal*, 121(15):2952–2961, 2022.
- [8] Masato Makino and Masao Doi. Brownian motion of a particle of general shape in newtonian fluid. *Journal of the Physical Society of Japan*, 73(10):2739–2745, 2004.
- [9] Sophie G Martin, W Hayes McDonald, John R Yates, and Fred Chang. Tea4p links microtubule plus ends with the formin for3p in the establishment of cell polarity. *Developmental cell*, 8(4):479–491, 2005.
- [10] Shane G McNally, Jane Kondev, and Bruce L Goode. Scaling of subcellular actin structures with cell length through decelerated growth. *Elife*, 10:e68424, 2021.

- [11] Lishibanya Mohapatra, Thibaut J Lagny, David Harbage, Predrag R Jelenkovic, and Jane Kondev. The limiting-pool mechanism fails to control the size of multiple organelles. *Cell systems*, 4(5):559–567, 2017.
- [12] Thomas D Pollard. Regulation of actin filament assembly by arp2/3 complex and formins. *Annu. Rev. Biophys. Biomol. Struct.*, 36:451–477, 2007.
- [13] Aldric Rosario, Shane G McNally, Predrag R Jelenkovic, Bruce L Goode, and Jane Kondev. Universal length fluctuations of actin structures found in cells. *bioRxiv*, pages 2023–07, 2023.
- [14] Aaron D Rosenbloom, Elizabeth W Kovar, David R Kovar, Leslie M Loew, and Thomas D Pollard. Mechanism of actin filament nucleation. *Biophysical Journal*, 120(20):4399–4417, 2021.
- [15] Jeremy D Rotty and James E Bear. Competition and collaboration between different actin assembly pathways allows for homeostatic control of the actin cytoskeleton. *Bioarchitecture*, 5(1-2):27–34, 2015.
- [16] Tom Shemesh, Takanori Otomo, Michael K Rosen, Alexander D Bershadsky, and Michael M Kozlov. A novel mechanism of actin filament processive capping by formin: solution of the rotation paradox. *The Journal of cell biology*, 170(6):889–893, 2005.
- [17] Cristian Suarez and David R Kovar. Internetwork competition for monomers governs actin cytoskeleton organization. *Nature reviews Molecular cell biology*, 17(12):799–810, 2016.
- [18] Cristian Suarez, Patrick M McCall, Margaret L Gardel, and David R Kovar. When is “enough” enough? *Cell systems*, 4(5):480–482, 2017.